Analytical Modelling and Simulation of Single and Double Cone Pinholes for Real-Time In-Body Tracking of a HDR Brachytherapy Source

Saree Alnaghy, Mitra Safavi-Naeini, Daniel R. Franklin, *Member, IEEE,* Zhangbo Han, Dean L. Cutajar, Marco Petasecca, *Member, IEEE,* Michael Lerch *Member, IEEE,* and Anatoly B. Rosenfeld *Senior Member, IEEE*

***Abstract*—The choice of pinhole geometry is a critical factor in the performance of pinhole-collimator-based source tracking systems for brachytherapy QA. In this work, an analytical model describing the penetrative sensitivity of a single-cone pinhole collimator to photons emitted from a point source is derived. Using existing models for single-cone resolution and double-cone sensitivity and resolution, the theoretical sensitivity and resolution of the single-cone collimator are quantitatively compared with those of a double-cone collimator with an equivalent field of view. Monte Carlo simulations of the single and double-cone pinhole collimators using an accurate 3D model of a commercial high dose rate brachytherapy source are performed to evaluate the relative performance of each geometry for a novel real-time HDR brachytherapy QA system, *H*DR BrachyView. The theoretical penetrative sensitivity of the single-cone pinhole is shown to be higher than the double-cone pinhole, which is in agreement with the results from the Monte Carlo simulations. The wider pinhole response function of the single-cone collimator results in a larger total error between the projected centre of the source and the estimated centre of mass of the source projection for the single-cone collimator, with the greatest error (at the maximum FoV angle) being 0.54 mm for the double-cone pinhole and 1.37 mm for the single-cone at $\theta = 60^{\circ}$. The double-cone pinhole geometry is determined to be the most appropriate choice for the pinhole collimator in the *H*DR BrachyView probe.**

***Index Terms*—Brachytherapy, source tracking, prostate cancer, analytical modelling, Monte Carlo simulations, pinhole collimators, imaging probe.**

I. Introduction

Pinhole photon collimators are a critical element of many X-ray/gamma-ray imaging systems, and are found in applications ranging from diagnostic equipment such as high resolution single photon emission computed tomography (SPECT) cameras, to quality assurance (QA) systems for radioactive source tracking in brachytherapy [1, 2, 3, 4]. Accurate analytical modelling of the imaging properties of pinhole is essential for optimising the design of such collimators for their specific applications.

The two key metrics for pinhole collimator performance are spatial resolution and sensitivity [5, 6]. Spatial resolution quantifies the smallest spatial feature which can be resolved using a given imaging system, while the sensitivity of a pinhole camera is defined as the fraction of photons emitted by the source which reach the imaging plane. Pinhole sensitivity includes two components: a geometric term, which accounts for the photons that pass directly through the physical aperture and are not subject to attenuation, and a penetration term, which accounts for the photons that pass through the attenuating medium from which the collimator is fabricated.

Several models have previously been proposed for a variety of pinhole types and imaging applications.

Jansen et al. introduced a geometric model for multiple keel-edge pinhole collimators in a conventional gamma camera system [7]. The model is used to solve the problem of overlapping projections and to jointly optimise the sensitivity and resolution.

Accorsi and Metzler have previously described an analytical model for the spatial resolution and sensitivity of a *d*ouble-cone pinhole design [5, 6]. The derived pinhole resolution model is known as the *r*esolution equivalent effective diameter, d_{re}, and is defined as the diameter of an *i*deal pinhole fabricated from a perfectly radiation-opaque material which provides a geometric resolution equivalent to that of the real pinhole, but with a larger diameter that models the effects of photon penetration. The model for penetrative sensitivity is derived by determining the path length of incident photons emitted from an ideal point source (i.e. those photons which penetrate the surface of the collimator) and integrating the attenuated flux over all such points. It assumes that all photons with more than a certain angle of incidence are stopped within the collimator due to the thickness of material that they must traverse.

Huang et al. investigate analytical modelling of a finite aperture for small animal pinhole SPECT imaging [8]. The developed model describes the probability that a single photon emitted from the radiation source is detected on the imaging plane. The probability of photon detection is calculated based on the cross sectional intersection area from the source passing through the aperture and reaching the detector plane.

Bal and Acton derived an analytical model to characterise the sensitivity and resolution of a pinhole collimator [9]. The point spread function (PSF) was derived for two pinhole geometries: right-circular double-cone and oblique-circular double-cone. The methodology used to derive the pinhole sensitivity was the sum of the geometric and penetrative sensitivity components. The geometric part is determined based on the physical parameters of the pinholes. The penetrative term requires calculating the path length of photons

S. Alnaghy, M. Safavi-Naeini, Z. Han, D.L. Cutajar, M. Petasecca, M. Lerch and A.B. Rosenfeld are with the Centre for Medical Radiation Physics, University of Wollongong, Wollongong, NSW 2522 Australia.

D.R. Franklin is with the School of Computing and Communications, University of Technology Sydney, NSW 2007 Australia.

passing through the pinhole material subject to attenuation and exiting out the end of the aperture. It was demonstrated that for low to medium-energy photons, the PSF for the oblique-circular double-cone produced well-defined symmetric projections with the centre of mass of the projection closely correlated with the proper geometric projection of the centre of the source. However, with higher-energy photons, the resulting PSF exhibited significant asymmetry. The right-circular double-cone geometry resulted in an asymmetric PSF for all photon energies. For a small aperture, the right circular double-geometry resulted in fewer penetrated photons and a more compact PSF, making it ideal for high resolution imaging systems. However, the study does not extend the model to a include single-cone geometries, which is a common pinhole model used in imaging systems.

In this paper, the analytic model for the sensitivity of a double-cone collimator (originally introduced by Metzler et al. [6]) is extended to a single-cone pinhole geometry. The model is validated against Monte Carlo simulations and used to determine the optimal choice of pinhole design for a collimator to be used in a novel QA system for high dose rate (HDR) prostate brachytherapy.

The extension to the analytical sensitivity model of Metzler et al. is derived in Section II. The system for which the models have been developed, High Dose Rate (HDR) *B*rachyView, is a recently-proposed QA system for real-time in-body imaging of an HDR prostate brachytherapy source. The design and source localisation method together with the simulated and experimental charactersiation of the device have been previously reported [3, 10, 11]. In brief, the device is composed of a tungsten pinhole collimator and an array of high-resolution silicon photodetectors enclosed within a transrectal probe. Images of the source are projected through each pinhole onto the detector plane, automatically segmented, and the centres of mass of the projections are back-projected through the corresponding pinholes. An estimate of the three-dimensional source position is determined by finding the point in space with minimum mean squared distance to all of the backprojected rays. As there are seven pinholes, a unique solution exists provided that at least two projections are visible; however, the quality of the estimate improves with the number of visible projections. The anatomical position of the source is found by co-registering the probe's coordinate system with the transrectal ultrasound (TRUS) system.

The probe is described in detail in Section II. The analytical predictions for spatial resolution and sensitivity for both single and equivalent double pinhole geometries are compared in Section III; the specific analytical results presented are based on a symmetric double-cone structure with a cylindrical connecting channel as shown in Figure 1(a) and a single-cone structure with a wider full acceptance angle, again connected to the bottom of the collimator by a small cylindrical channel as shown in Figure 1(b).

Results from Monte Carlo simulations of *H*DR BrachyView with single and double pinhole collimators with the same geometry as the analytic comparison are presented in Section III. The analytic performance predictions for both designs are compared with the Monte Carlo simulation results in order to determine the best pinhole geometry for *H*DR BrachyView. In Section IV, it is shown that the double-cone pinhole design provides a superior spatial resolution with an acceptable reduction in sensitivity, making it the preferred design for *H*DR BrachyView. Section V summarises our findings and describes the next steps in this project.

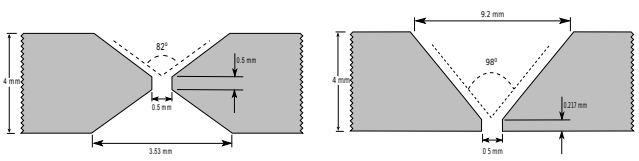

(a) Double cone (b) Single cone

Fig. 1. Pinhole geometries proposed for the *H*DR BrachyView probe

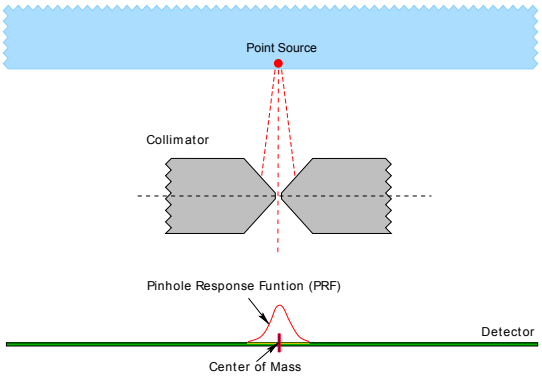

Fig. 2. The pinhole response function (PRF): distribution of photons on the imaging plane; its FWkM is used as a measure of its resolution

II. Materials and Methods

A. Analytical Computation of Pinhole Resolution and Sensitivity

The most important characteristics of a pinhole collimator are sensitivity and spatial resolution, both of which would be ideally as high as possible. However, there is an intrinsic trade-off between sensitivity and spatial resolution [2]. Increasing the acceptance angle of a pinhole collimator will increase the sensitivity to photon detection (and also the width of the field of view), but degrades the spatial resolution since the ratio of direct photons (photons that travel through the aperture of the pinhole) to penetrated photons (photons that penetrate through the tungsten collimator) decreases.

1) Resolution: Spatial resolution can be determined by finding the full width at kth maximum (FWkM) of the PSF or line spread function (LSF) of the imaging system. In the case of a pinhole camera, resolution is defined as the width of the pinhole response function (PRF) exceeding a fraction (k) of its maximum value (typically half, i.e. $k = 0.5$). The PRF is the 2D spatial distribution of the photons which are emitted by the point source, pass through the collimator and reach the imaging plane, as shown in Figure 2 [6, 12].

For an ideal pinhole with diameter d and a magnification factor M (defined as the ratio of projection size to the size of the original object), the resolution (λ) corresponding to the full width at half maximum (FWHM) is given by [13]:

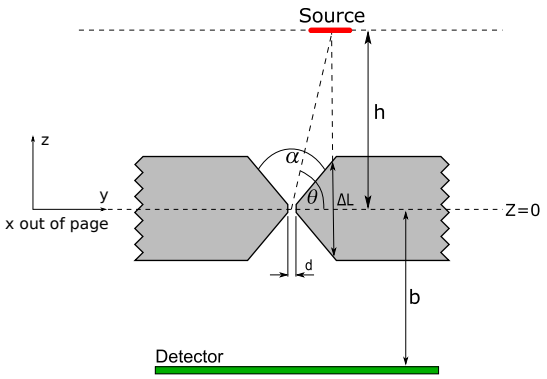

Fig. 3. Parameters of a pinhole collimator: The pinhole has a diameter d with a full acceptance angle α. A photon source, offset at angle θ to the y-axis at a distance h from the pinhole centre, projects onto the imaging plane. ΔL represents the path length of penetrated photons inside the collimator.

$$\lambda = d\left(1 + \frac{1}{M}\right) \tag{1}$$

A more general metric for quantifying pinhole resolution of a pinhole fabricated from a real material is the *r*esolution equivalent effective diameter, d_{re}, which accounts for the angular offset of the point source with respect to the central axis of the pinhole [5, 6]. By definition, the PRF (and its corresponding FWkM) is directly proportional to its resolution equivalent diameter (d_{re}); that is, as d_{re} increases, pinhole resolution deteriorates (numerically increases, i.e. the PRF distribution broadens).

The parameters of the double-cone pinhole geometry are shown in Figure 3; parameter names are as for the single-cone pinhole geometry. ΔL represents the total distance inside the collimator traversed by penetrating photons before they are projected onto the imaging plane, i.e. the path length of photons that penetrate through the solid body of the collimator.

ΔL is a function of the polar radius ρ, and the azimuthal angle ϕ of the point source relative to the x-axis, shown in Figure 4(b). The figure shows the photons emitted by the point source (shown as the larger solid circle) passing through and leaving the collimator on the $z = 0$ plane (smaller solid circle). Due to azimuthal symmetry, ϕ may be assumed to be zero, which simplifies the problem without decreasing the generality of the result. The path length can be expressed as follows:

$$\Delta L = -\frac{\ln k}{\mu} \equiv \Delta L_k \tag{2}$$

where k determines the fraction value of the full width at k^{th} maximum of the PRF and μ is the linear attenuation coefficient of the medium.

2) Sensitivity: Pinhole sensitivity can be described mathematically as:

$$S_{total}(\theta) = S_{geom}(\theta) + S_{pen}(\theta) \tag{3}$$

where $S_{geom}(\theta)$ is the angle-dependent geometric sensitivity, which represents the fraction of incident photons that pass directly through the physical aperture and $S_{pen}(\theta)$ is the penetrative sensitivity, which represents the fraction of photons passing through the attenuating medium of the collimator.

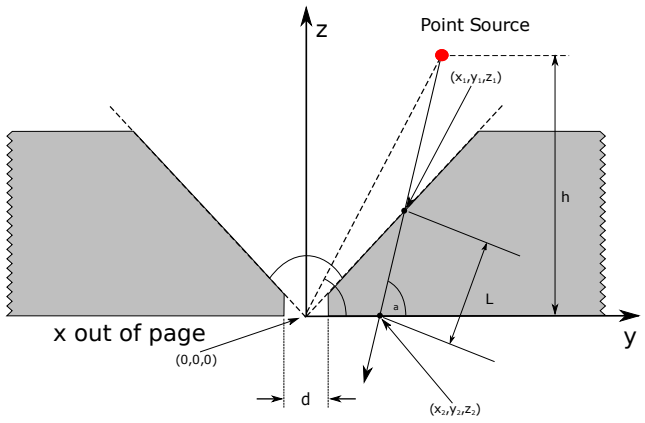

(a) 2D view

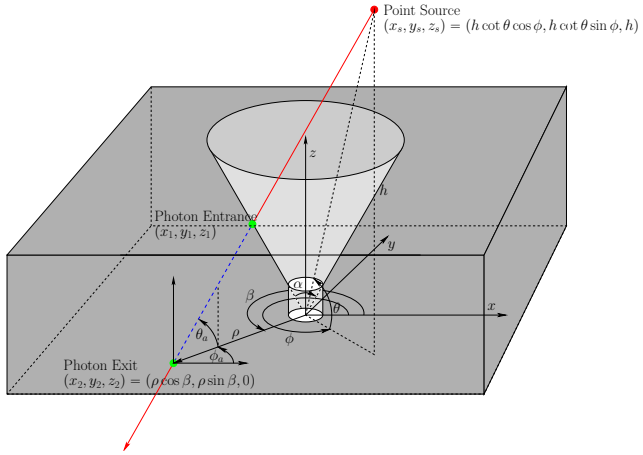

(b) 3D view

Fig. 4. Single cone pinhole collimator, showing all key geometric parameters

The penetrative sensitivity for a double-cone pinhole collimator has been derived by Metzler et al. as follows [6]:

$$S_{pen}(\theta) \approx \frac{\sin^5\theta\tan^2\frac{\alpha}{2}}{8h^2\mu^2} \times \left(1 - \frac{\cot^2\theta}{\tan^2\frac{\alpha}{2}}\right)^{1/2} \times \left[1 - \frac{\cot^2\theta}{\tan^2\frac{\alpha}{2}} + \mu d\csc\theta\cot\frac{\alpha}{2}\right] \tag{4}$$

An equivalent expression for penetrative sensitivity can be derived for a single-cone pinhole. $S_{pen}(\theta)$ is again dependent on the path length through the collimator's body. To calculate $S_{pen}(\theta)$, it is assumed that photons radiate from a point source in a spherical coordinate system. The path length of a photon penetrating the collimator at a fixed point is calculated. The path length is then calculated relative to the two points of intersection, (x_1, y_1, z_1) and (x_2, y_2, z_2), shown in Figure 4(a), which is represented as (θ_a, ϕ_a) and parameterised relative to the reference frame of the origin $(x, y, z) = (0, 0, 0)$ represented as (θ, ϕ). The expression is then expanded, simplified and integrated using (5). The method adopted in this paper is similar to that derived by Metzler et al. for a double-cone

pinhole design [6]. A general expression for the penetrated photon sensitivity is given by

$$S_{pen}(\theta) = \frac{\sin^3\theta}{4\pi h^2}\int_0^{2\pi}\int_{\frac{d}{2}}^{\infty}\rho e^{-\mu\Delta L}d\rho d\beta \tag{5}$$

where the integrand is the photon flux incident on the projection of an infinitesimal area $dA = \rho d\beta \cdot d\rho$ (on the $z = 0$ plane) onto a sphere of radius $h/\sin\theta$ originating at the point source, after attenuation through a section of material with linear attenuation μ of path length ΔL. The key problem is to determine an expression for the path length ΔL for a given cone geometry.

Figure 4(a) shows the Euclidean path length ΔL between the point of photon ingress and egress on the single-cone pinhole collimator in a spherical coordinate system, assuming the point source to be within the extended projection of the cone (if a source is outside this region, the pinhole can be ignored as any penetrating photons will traverse at least the total thickness of the collimator plate, with a very high probability of absorption).

The points shown in (6) and (7) represent the upper and lower points of intersection respectively between a penetrating photon's trajectory and the body of the collimator. Equation (8) is the formula of a cone; hence the expressions for x_1 and y_1 in terms of z_1 may be substituted for x and y in (8) and rearranged to yield a quadratic equation in terms of z_1, which can be solved to yield two solutions.

$$\begin{aligned}(x_1, y_1, z_1) = (&\rho\cos\beta + z_1\cot\theta_a\cos\phi_a,\\ &\rho\sin\beta + z_1\cot\theta_a\sin\phi_a,\\ &z_1)\end{aligned} \tag{6}$$

$$(x_2, y_2, z_2) = (\rho\cos\beta, \rho\sin\beta, 0) \tag{7}$$

$$x^2 + y^2 = \left(z\tan\frac{\alpha}{2} \pm \frac{d}{2}\right)^2 \tag{8}$$

To simplify the analysis, it is assumed that $d = 0$. This does not significantly affect the penetrated photon distribution as the maximum thickness of the collimator is only 0.2 mm at the point where the channel is drilled, so attenuation of photons in this region is negligible. The expression for z_1 with $d = 0$ yields:

$$z_1 = \frac{-\rho\cos(\beta-\phi_a)\cot\theta_a + \sqrt{\begin{aligned}&\rho^2\cos^2(\beta-\phi_a)\cot^2\theta_a\\ &-\rho^2\cot^2\theta_a + \rho^2\tan^2\frac{\alpha}{2}\end{aligned}}}{\cot^2\theta_a - \tan^2\frac{\alpha}{2}} \tag{9}$$

Now, calculating the Euclidean distance between the two points of intersection (x_1, y_1, z_1) and (x_2, y_2, z_2) to find ΔL:

$$\Delta L^2 = z_1^2\cot^2\theta_a\cos^2\phi_a + z_1^2\cot^2\theta_a\sin^2\phi_a + z_1^2 \tag{10}$$

Substitution of (9) into (10) yields an expression for ΔL:

$$\Delta L = \frac{\rho\csc\theta_a\left(\sqrt{\begin{aligned}&\tan^2\frac{\alpha}{2} - \cot^2\theta_a\sin^2(\beta-\phi_a)\\ &-\cot\theta_a\cos(\beta-\phi_a)\end{aligned}}\right)}{\cot^2\theta_a - \tan^2\frac{\alpha}{2}} \tag{11}$$

The path length needs to be expressed in terms of θ and ϕ, the elevation and azimuth of the point source relative to the aperture. Equation (11) is then expressed in terms of absolute source elevation and azimuth angles (θ, ϕ) using the same trigonometric relations used by Metzler et al. [6]; due to azimuthal symmetry, ϕ may be assumed to be zero, resulting in (12):

$$\begin{aligned}\Delta L = &\frac{\sqrt{\frac{\rho^2}{h^2} - 2\frac{\rho}{h}\cos\beta\cot\theta + \csc^2\theta}}{-(\tan^2\frac{\alpha}{2} - \frac{\rho^2}{h^2} + 2\frac{\rho}{h}\cos\beta\cot\theta - \cot^2\theta)}\times\\ &\left[\rho\sqrt{\tan^2\frac{\alpha}{2} - \sin^2\beta\cot^2\theta} - \rho\cos\beta\cot\theta + \frac{\rho^2}{h}\right]\end{aligned} \tag{12}$$

Since $\rho \ll h$ (as it is assumed that the point source is inside the projection of the pinhole cone), we can use the approximation $\frac{\rho^2}{h^2} \approx 0$. The numerator and denominator of (12) are then expanded in terms of $\frac{\rho}{h}$, resulting in (13):

$$\begin{aligned}\Delta L &\approx \frac{\csc\theta\left(1 - \frac{\rho}{h}\cos\beta\sin\theta\cos\theta\right)}{\cot^2\theta - \tan^2\frac{\alpha}{2}}\times\\ &\frac{\sqrt{\rho^2\tan^2\frac{\alpha}{2} - \rho^2\sin^2\beta\cot^2\theta} - \rho\cos\beta\cot\theta + \frac{\rho^2}{h}}{2\frac{\rho}{h}\frac{\cos\beta\cot\theta}{\tan^2\frac{\alpha}{2} - \cot^2\theta} + 1}\\ &= \frac{\csc\theta\left(1 - \frac{\rho}{h}\cos\beta\sin\theta\cos\theta\right)\left(1 - 2\frac{\rho}{h}\frac{\cos\beta\cot\theta}{\tan^2\frac{\alpha}{2} - \cot^2\theta}\right)}{\cot^2\theta - \tan^2\frac{\alpha}{2}}\times\\ &\left(\sqrt{\rho^2\tan^2\frac{\alpha}{2} - \rho^2\sin^2\beta\cot^2\theta} - \rho\cos\beta\cot\theta + \frac{\rho^2}{h}\right)\\ &= \frac{\csc\theta\left(1 - 2\frac{\rho}{h}\frac{\cos\beta\cot\theta}{\tan^2\frac{\alpha}{2} - \cot^2\theta} - \frac{\rho}{h}\cos\beta\sin\theta\cos\theta\right)}{\cot^2\theta - \tan^2\frac{\alpha}{2}}\times\\ &\left(\sqrt{\rho^2\tan^2\frac{\alpha}{2} - \rho^2\sin^2\beta\cot^2\theta} - \rho\cos\beta\cot\theta + \frac{\rho^2}{h}\right)\end{aligned} \tag{13}$$

Expanding (13) and assuming all second order $\frac{\rho^2}{h^2}$ terms to be negligible, results in the following approximation for ΔL:

$$\begin{aligned}\Delta L \approx &\frac{\rho\csc\theta\left(\sqrt{\tan^2\frac{\alpha}{2} - \sin^2\beta\cot^2\theta} - \cos\beta\cot\theta\right)}{\cot^2\theta - \tan^2\frac{\alpha}{2}}\times\\ &\left(-2\frac{\rho}{h}\frac{\cos\beta\cot\theta}{\tan^2\frac{\alpha}{2} - \cot^2\theta} - \frac{\rho}{h}\cos\beta\sin\theta\cos\theta + 1\right)\end{aligned} \tag{14}$$

Since $\int_0^{2\pi}\cos\beta d\beta = 0$, each of the terms in (14) with a $\cos\beta$ factor will become zero after integration with respect to β. Equation (14) therefore reduces to:

$$\Delta L \approx \frac{\rho\csc\theta\sqrt{\tan^2\frac{\alpha}{2} - \sin^2\beta\cot^2\theta}}{\cot^2\theta - \tan^2\frac{\alpha}{2}} \tag{15}$$

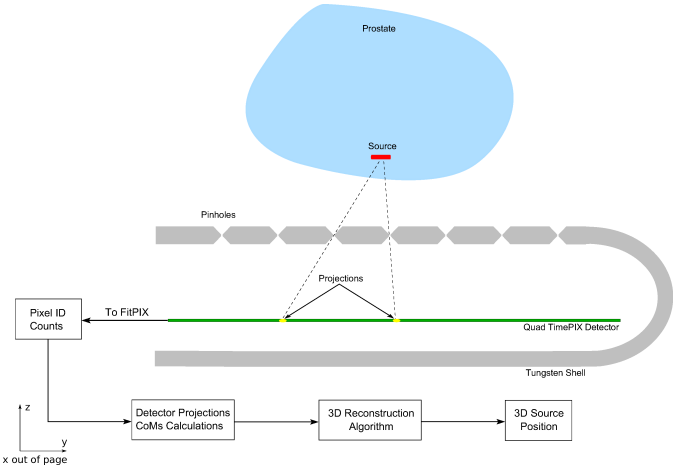

Fig. 5. Conceptual diagram of *H*DR BrachyView imaging system.

(15) can now be integrated using (5).

$$S_{pen}(\theta) \approx \frac{\sin^3\theta}{4\pi h^2}\int_0^{2\pi} d\beta \times \int_0^{\infty} \rho \exp\left[-\mu \frac{\rho \csc\theta \sqrt{\tan^2\frac{\alpha}{2} - \sin^2\beta\cot^2\theta}}{\cot^2\theta - \tan^2\frac{\alpha}{2}}\right] d\rho \approx \frac{\sin^3\theta}{4\pi h^2}\left[\frac{\sec^4\frac{\alpha}{2}\csc^2\theta(\cos\alpha+\cos 2\theta)^2}{4\mu^2\left(\tan^2\frac{\alpha}{2} - \sin^2\beta\cot^2\theta\right)}\right]\int_0^{2\pi} d\beta \tag{16}$$

Finally, integrating with respect to β results in an approximate expression for the sensitivity due to penetration for a single-cone pinhole collimator (17):

$$S_{pen}(\theta) \approx \frac{\sin^3\theta}{8\pi h^2\mu^2}\sec^4\frac{\alpha}{2}\csc^2\theta(\cos\alpha+\cos 2\theta)^2 \times \int_0^{2\pi} \frac{d\beta}{\tan^2\frac{\alpha}{2} - \sin^2\beta\cot^2\theta} = \frac{\tan^2\frac{\alpha}{2}\sin^5\theta}{4\sqrt{2}h^2\mu^2}\left[-\csc^2\frac{\alpha}{2}\csc^2\theta(\cos\alpha+\cos 2\theta)\right]^{3/2} \tag{17}$$

B. The HDR BrachyView Real-time QA Imaging System

A novel real-time QA system for real-time in-body tracking of a HDR prostate brachytherapy source, *H*DR BrachyView, is currently under development at the University of Wollongong Center for Medical Radiation Physics (CMRP) in parallel with a related low dose rate (LDR) version [3, 4, 11]. This transrectal source-monitoring system for HDR brachytherapy uses projections of the source through multiple pinholes in a tungsten collimator onto a pixelated silicon detector to track the source position in real time. The centres of mass (CoMs) for each projection are then located, and a line from each of the CoMs is backprojected through the corresponding pinhole collimator. The source location is found by finding the point in space with the minimum mean squared distance to all back-projected lines. The imaging area consists of four TimePix detectors, each with an individual sensitive area of 15 mm×15 mm divided into an array of 256×256 pixels [14, 15]. The total imaging area that will be used as the rectal probe is 15 mm×56 mm with a total of 256×1024 pixels. The system needs to be able to track and image an ^{192}Ir source anywhere within the nominal prostate volume of 40×40×40 mm^3 shown in Figure 5. In *H*DR BrachyView, the distance between the probe and the source may be as Little as 5 mm; additionally, the mean energy of the ^{192}Ir source is 380 keV, which is highly penetrating. Consequently, the collimator needs to provide as much attenuation as possible; however, due to space constraints inside the *H*DR BrachyView probe, the maximum feasible thickness is 4 mm. A commercially available tungsten alloy (95% W, 3.5% Ni and 1.5%Cu) was chosen as the material for the collimator, since a 4 mm thick collimator fabricated from this alloy blocks approximately 80% of incident 380 keV photons.

The collimator used in the QA probe employs conical pinholes with a truncated knife-edge geometry. Two alternative pinhole geometries were investigated: the first is a symmetric double-cone design, where the cones are connected by a small cylindrical channel; the second uses a single cone with a wider acceptance angle connected to the bottom face by a small cylindrical channel as. The double and single cone pinholes are shown in Figures 1(a) and 1(b), respectively. Both pinhole designs have a connecting channel diameter of $d = 0.5$ mm. The acceptance angles (α) for the double and single-cone pinholes were set to 82° and 98° respectively; these angles allow the entire sensitive surface of the detector array to be used, given the geometric constraints of the rectal probe, and provide good visibility to more than 70% of the prostate volume. The remaining regions (at the bottom of the prostate volume on either side of the y axis) can be monitored (if necessary) by rotating the probe either clockwise or anticlockwise. The acceptance angles were calculated by projecting lines from the corners of the detector through the collimator at the base of the pinhole channel. The acceptance angle is calculated using (18), where b is the distance between the pinhole and detector and x is the distance between the centre of pinhole on the detector plane and the edge of the detector.

$$\alpha = 2\tan^{-1}\left(\frac{x}{b}\right) \tag{18}$$

d_{re} for the double-cone (d_{re}^{dc}) and single-cone (d_{re}^{sc}) pinholes are given by the respective approximations:

$$d_{re}^{dc} \approx d - \frac{\ln k}{\mu}\left(\tan^2\frac{\alpha}{2} - \cot^2\theta\right)\cot\frac{\alpha}{2}\sin\theta \tag{19}$$

$$d_{re}^{sc} \approx d - 2\frac{\ln k}{\mu}\sin\theta\tan\frac{\alpha}{2} \tag{20}$$

C. Monte Carlo Simulations

Monte Carlo simulations of the double-cone and single-cone pinhole geometries were performed, based on the design of the *H*DR BrachyView system described in Section II-B. A

tungsten alloy plate with conical pinholes and an ^{192}Ir source were modelled in Geant4. The simulated source consists of a core made from an alloy of 10% ^{192}Ir and 90% platinum surrounded by a pure platinum shell; this structure is based on Alpha-Omega Services HDR ^{192}Ir source [16]. A pixelated silicon detector was placed 8.5 mm below the centre of the collimator. The source-to-pinhole height h for the double-cone and single-cone were set as 7 mm and 9 mm respectively. h is 2 mm greater for the single-cone pinhole simulation since the centre of the pinhole is shifted 2 mm lower compared to the double-cone pinhole.

Figure 6 shows the geometry of both the double-cone and single-cone simulations. Five source positions were simulated for each pinhole geometry, with the centre of the source located at $(\theta, \phi) = (60°, 0°)$, $(60°, 90°)$, $(75°, 0°)$, $(75°, 90°)$ and $(90°, 0°)$. The cases where $\theta = 60°$ represent the most extreme location of the source, where it is placed at the very edge of the pinhole FoV; $\theta = 90°$ represents the best-case scenario where the source is directly above the pinholes and $\theta = 75°$ is an intermediate value. For $\phi = 0$, the source is translated in a direction parallel to its major axis (that is, along the y-axis); for $\phi = 90°$, the source is moved in a direction perpendicular to its major axis (that is, along the x-axis). Four billion photon events were generated for each simulation; the photon energy distribution was generated based on the standard ^{192}Ir spectrum [16].

Monte Carlo simulations were performed to validate the analytical sensitivity models. The simulation scenario was configured similarly to the previous simulations, with two simplifications to match the assumptions used in the analytic model: firstly, the geometry of the pinholes was changed to a knife-edge design (i.e. the cylindrical channel was removed), and secondly, the HDR source was changed to a point source. The same source positions were simulated. The analytical models were reintegrated using (5) with a finite value of ρ to ensure that the RoI was within the detector FoV in the simulation.

III. Results

A. Analytical Computation of Pinhole Resolution and Sensitivity

1) Resolution: Using (19) and (20), the resolution equivalent diameter d_{re} for both double and single-cone pinholes was analytically determined for values of k between 0.1 and 1. The following parameters (as illustrated in Figure 1(a) and 1(b)) were used for both the double-cone and single-cone pinholes to analytically determine values of d_{re}^{DKE} and d_{re}^{SKE}. The analytical values of d_{re} were used to calculate the theoretical FWHM of the projections at the detector plane for both single-cone and double-cone pinhole geometries and were compared to the FWHMs of the projected images obtained from the simulation.

The linear attenuation coefficient (μ) was assumed to be approximately 5.2 ± 0.1 cm^{-1} for tungsten at 380 keV. d_{re} was determined at the three source angles chosen from the Monte Carlo simulations, 60°, 75° and 90°, for both pinhole geometries.

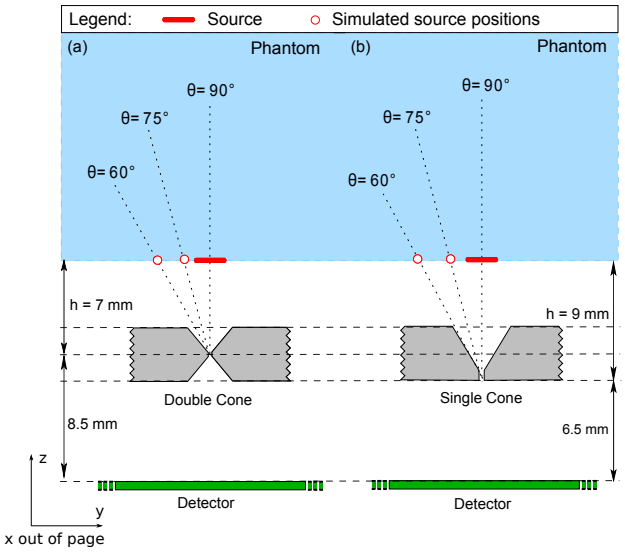

Fig. 6. The simulated positions of the source, collimator, phantom and detector for the double-cone pinhole (a) and the single-cone pinhole (b). The illustration shows the source being translated along the y-axis (i.e. $\phi = 0°$); a similar translation is separately performed along the x-axis ($\phi = 90°$), for a total of 5 source positions (at the same vertical distance above the collimator and detector).

Graphs showing the analytical estimates of resolution-equivalent diameter for both double-cone and single-cone pinhole geometry are shown in Figure 7.

2) Sensitivity: Analytical expressions for double-cone and single-cone pinhole sensitivity ((4) and (17) respectively) are normalised to their respective source-to-collimator distance (h_{DKE}, h_{SKE}) and plotted as functions of horizontal source displacement y with vertical source-to-pinhole distances $h_{DKE} = 7,\ 23,\ 43$ mm (or $h_{SKE} = 9,\ 25,\ 45$ mm for the single cone geometry) as shown in Figures 8(a), 8(b) and 8(c), respectively.

B. Monte Carlo Simulation

Images of the ^{192}Ir source model projected through the simulated double-cone and single-cone pinhole collimators, generated using 4 billion photon events, are shown in Figure 9. Each figure illustrates the projection of the HDR source onto a single 256 × 256 pixel detector array. The source was simulated at the five locations $(\theta, \phi) = (60°, 0°)$, $(60°, 90°)$, $(75°, 0°)$, $(75°, 90°)$ and $(90°, 0°)$ for both pinhole geometries. One-dimensional image profiles were obtained across the centre of the projection (along the x-axis). As the underlying function is known to be smooth and continuous, a Savitsky-Golay filter was applied to the profiles to reduce noise and smooth the profile without distorting its underlying shape; the original and smoothed signals are shown in Figure 10.

The full width at k^{th} maximum of the smoothed PRFs were measured directly. The FWkM was then plotted against each value of k for the double-cone and single-cone pinhole for three values of θ as shown in Figure 11.

Figures 12(a) and 12(b) display the analytical and simulated penetrative sensitivity of the double and single-cone pinholes, respectively. The analytical models were integrated using a

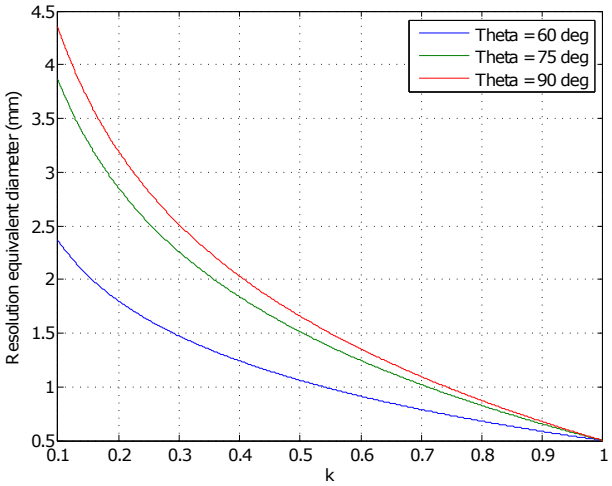

(a) Double cone

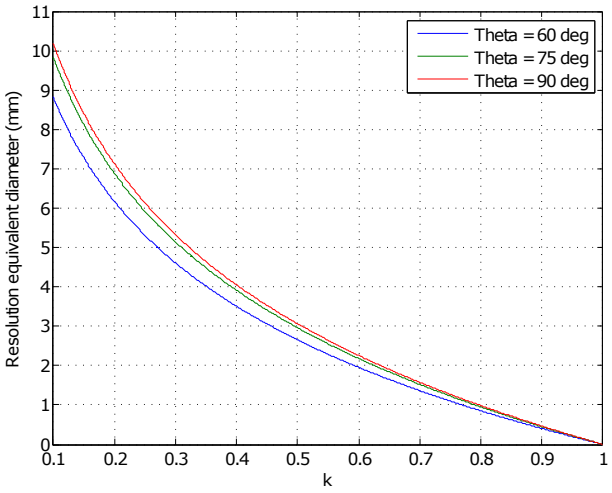

(b) Single cone

Fig. 7. Analytical estimate of the resolution-equivalent diameters d_{re}^{DKE} and d_{re}^{SKE} for double and single-cone pinholes, respectively. The full widths at kth maximum are shown for k between 0.1 and 1, for source positions $\theta = 90°$, $75°$ and $60°$ ($\phi = 0°$).

finite value of ρ as the upper limit. This value was calculated to achieve a RoI covering the detector plane once integrated over the azimuthal angle. The same RoI was used for both geometries. The sensitivity from the simulations was then calculated by integrating over the same RoI on the detector plane. Both data sets were normalised at $\theta = 90°$. The confidence intervals in the simulations represent $\pm 3\sigma$ (99.7% confidence).

IV. Discussion

A. Analytical Calculations

From Figure 7, it may be observed that d_{re} for the double-cone pinhole is consistently smaller than the value for the single-cone pinhole for each case of $\theta = 90°$, $75°$ and $60°$. Therefore, it is concluded that, in general, the double-cone pinhole geometry has a narrower PRF and hence will block a larger fraction of high-energy photons close to the aperture compared to an equivalent single-pinhole geometry. The FWHM ($k = 0.5$) for the double-cone has a d_{re} of 1.7 mm compared with the FWHM of the single-cone with a d_{re} value of 3.10 mm at $\theta = 90°$. For both designs, when the source is placed directly above the collimator (i.e. $\theta = 90°$), d_{re} is at its maximum. This is due to the large photon flux in the neighbourhood of the aperture and hence higher photon penetration through the collimator around the pinhole. This broadens the PRF and degrades the spatial resolution. As the source moves away from the pinhole i.e at $\theta = 75°$ and $\theta = 60°$, fewer photons penetrate around the aperture of the pinhole, creating a slightly narrower PRF and improving the spatial resolution.

Figures 8, shows the theoretical penetrative sensitivity for the double-cone and single-cone pinhole geometries as a function of horizontal source displacement in the y direction (moving towards the edge of the FoV as y increases). The penetrative sensitivity term was derived analytically by assuming the path length of incident photons through the collimator are as for an ideal point source; however, the source used in *H*DR BrachyView has a physical length of 3 mm and therefore cannot be accurately modelled as a point source, particularly when the source is close to the collimator. Sensitivity varies across the length of the source, and hence the relative sensitivity is much greater for the single-cone compared with the double-cone pinhole because the sensitivity of the double-cone decreases more rapidly with horizontal displacement compared to the single-cone geometry.

B. Monte Carlo Simulation

The projection images from the simulated double-cone pinhole collimator exhibit a much sharper image of the source compared with the single-cone pinhole collimator, confirming the predicted analytical results for pinhole resolution. There is also less penetration close to the aperture of the double-cone pinhole compared with the single-cone case. The total number of photons for a given source activity and exposure time is greater with the single-cone pinhole geometry, therefore its sensitivity is better than the double-cone pinhole.

As the source moves away from the centre of the pinholes, the CoM of the projection shifts in the direction of the pinhole relative to the projected centre of the source (the point of intersection of the line drawn between the source centre and the pinhole apex with the detector plane). The differences between the CoMs of the projections and the projected source centres are summarised in Tables I and II for double-cone and single-cone pinholes, respectively. The shift increases for both pinholes as θ increases, since the source is not a point source; rather, it has a physical length of 3.6 mm and a width of 0.65 mm. This means that the end or side of the source that is closest to the pinhole contributes in a greater photon flux density on the imaging plane compared to the far end of the source. At $\theta = 60°$, the centre of the source is at the very edge of the FoV, which means that part of the source is actually *o*utside the FoV (either one end of the source, for $\phi = 0°$, or both ends of the source, for $\phi = 90°$). This is the main reason for the significantly higher shift relative to projected centre of source which is observed for both collimators at $(\theta, \phi) = (60°, 90°)$; however, the error is much greater for the

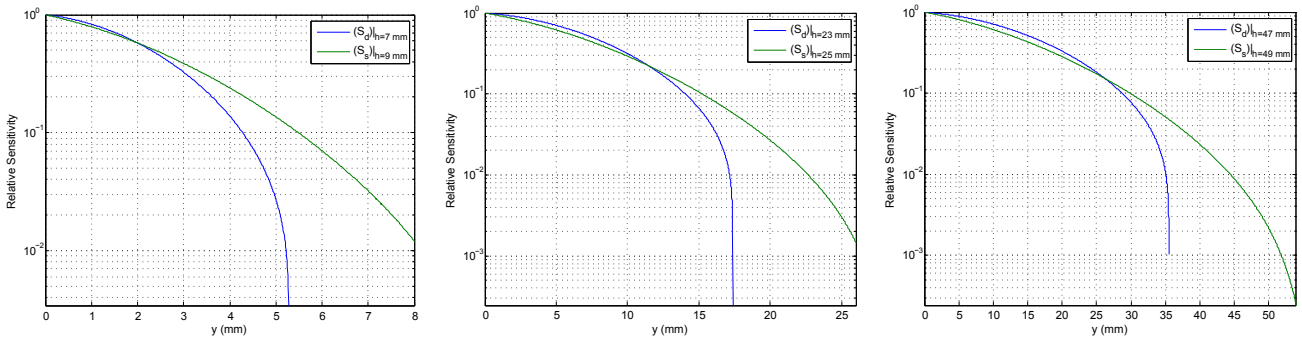

(a) $h_{DKE} = 7$ mm, $h_{SKE} = 9$ mm (b) $h_{DKE} = 23$ mm, $h_{SKE} = 25$ mm (c) $h_{DKE} = 43$ mm, $h_{SKE} = 45$ mm

Fig. 8. Analytical expressions for the penetrative sensitivity for double-cone and single-cone pinholes at various source-to-collimator distances, normalised to their respective source-to-collimator distance (h_{DKE}, h_{SKE}) and plotted against horizontal source displacement y, where $y = 0$ is the position directly above the centre of the pinhole.

TABLE I
LOCATION OF THE CENTRE OF THE SOURCE PROJECTED THROUGH THE CENTRE OF THE DOUBLE-CONE PINHOLE COMPARED TO THE LOCATION OF THE CENTRE OF MASS OF THE PROJECTED IMAGE.

Source position $(\theta,\ \phi)$	**Analytic**		**Simulation**		**Error**		
	x **(mm)**	y **(mm)**	x **(mm)**	y **(mm)**	Δx **(mm)**	Δy **(mm)**	Δd **(mm)**
90°, 0°	0	0	0.136	0.0285	0.136	0.0285	0.139
75°, 0°	0	2.28	0.00580	1.50	0.00580	0.776	0.776
60°, 0°	0	4.91	0.0900	3.44	0.09	1.47	1.47
75°, 90°	2.28	0	1.99	0.499	0.292	0.499	0.579
60°, 90°	4.91	0	4.38	0.127	0.529	0.127	0.544

TABLE II
LOCATION OF THE CENTRE OF THE SOURCE PROJECTED THROUGH THE CENTRE OF THE SINGLE-CONE PINHOLE COMPARED TO THE LOCATION OF THE CENTRE OF MASS OF THE PROJECTED IMAGE.

Source position $(\theta,\ \phi)$	**Analytic**		**Simulation**		**Error**		
	x **(mm)**	y **(mm)**	x **(mm)**	y **(mm)**	Δx **(mm)**	Δy **(mm)**	Δd **(mm)**
90°, 0°	0	0	0.128	0.0221	0.127	0.0221	0.130
75°, 0°	0	1.74	0.0545	1.10	0.0545	0.642	0.644
60°, 0°	0	3.75	0.120	2.33	0.09	1.42	1.43
75°, 90°	1.74	0	1.24	0.0442	0.500	0.0442	0.502
60°, 90°	3.75	0	2.41	0.226	1.35	0.226	1.37

single-cone case, since the difference in thickness of tungsten traversed by the out-of-FoV portion of the source on either side of the pinhole is greater than for the double-cone case. Therefore, the CoM of the projection at $(\theta, \phi) = (60°, 90°)$ is a better estimate of the projected centre of the source for the double-cone pinhole.

A smaller effect is also evident when the source is entirely within the FoV due to the differential free-space path length traversed by photons emitted from each end or each side of the source and passing directly through the pinhole aperture. This differential path length results in a differential photon flux at the two ends of the projection, causing its CoM to shift closer to the pinhole and introducing a small systematic error in the same direction as the source displacement. For both pinhole collimators, when $\theta = 90°$, the projected source centre and the CoM of the source projection are both directly below the pinhole. As the source is translated along the y-axis or x-axis, the difference in location of the projected source centre and the CoM of the simulated source projection increases by similar amounts for both pinhole collimators.

Figure 11 shows how the FWkM changes for different values of θ and confirms that the resolution of the double-cone pinhole geometry is also superior to that of the single-cone pinhole, as predicted by the analytical study. FWHMs measured with $\theta = 90°$ for the double-cone and single-cone pinholes were 4.63 mm and 7.98 mm, respectively. The difference in resolution is most pronounced when $\theta = 90°$. The theoretical FWHMs calculated at the detector plane were 3.10 mm and 7.15 mm for the double-cone and single-cone pinholes respectively. This compares well with the simulation results.

Figures 12(a) and 12(b) show that results from the analytical model for sensitivity are in good agreement with the simulation results for both geometries. However, as the source moves away from the centre of the pinholes, the analytical model begins to underestimate the penetrative sensitivity. This error is due to the assumption used in both models that all second order terms are negligible. In addition, the analytical

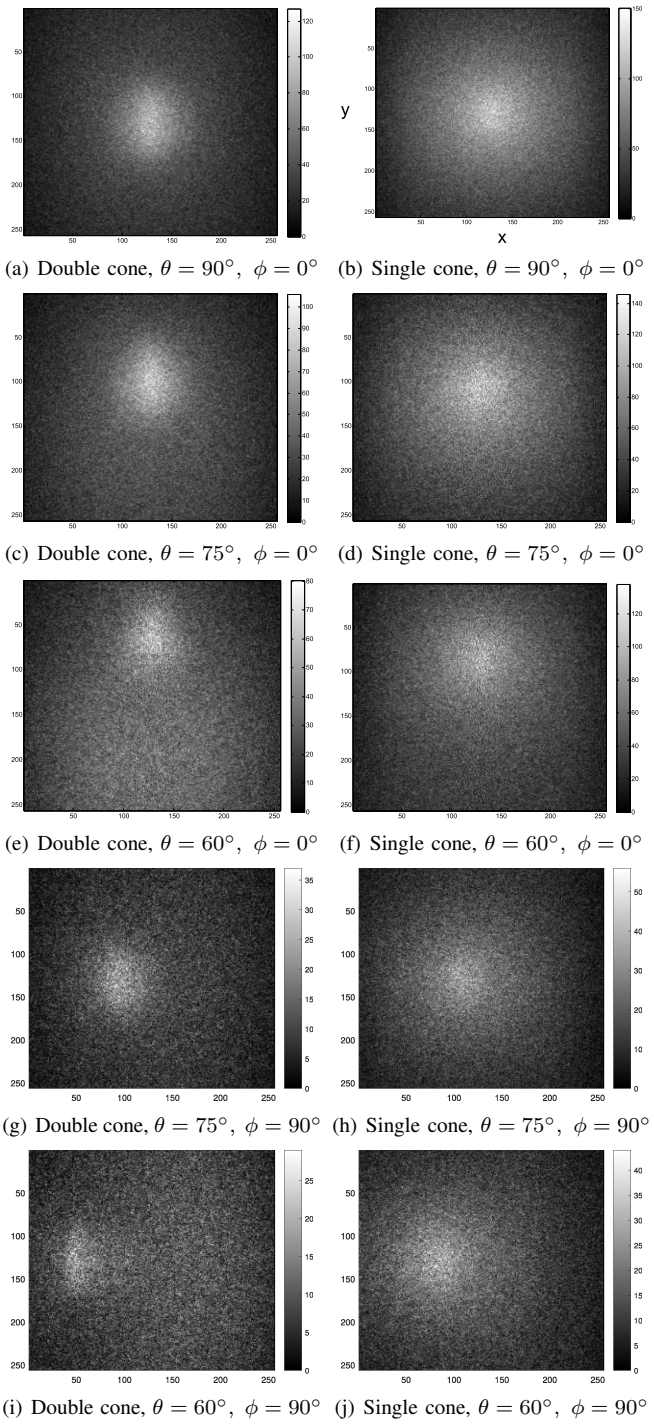

(a) Double cone, $\theta = 90°,\ \phi = 0°$ (b) Single cone, $\theta = 90°,\ \phi = 0°$

(c) Double cone, $\theta = 75°,\ \phi = 0°$ (d) Single cone, $\theta = 75°,\ \phi = 0°$

(e) Double cone, $\theta = 60°,\ \phi = 0°$ (f) Single cone, $\theta = 60°,\ \phi = 0°$

(g) Double cone, $\theta = 75°,\ \phi = 90°$ (h) Single cone, $\theta = 75°,\ \phi = 90°$

(i) Double cone, $\theta = 60°,\ \phi = 90°$ (j) Single cone, $\theta = 60°,\ \phi = 90°$

Fig. 9. Monte Carlo simulation of the projection of an image of a ^{192}Ir source located at $(\theta, \phi) = (60°, 0°)$, $(60°, 90°)$, $(75°, 0°)$, $(75°, 90°)$ and $(90°, 0°)$ passing through double-cone and single-cone pinholes onto a single 256×256 pixel detector array.

models assume that photons cannot penetrate the full thickness of the collimator. However, this is not the case in practice, as approximately 20% of the gamma photons from an ^{192}Ir source incident on a 4 mm thick tungsten slab will penetrate the collimator and reach the detector surface. The discrepancy between the models becomes larger as $\theta \to 0°$, since the ratio of the number of photons traversing the pinhole to the number penetrating the collimator body decreases as θ decreases.

V. Conclusion

An analytical model describing the sensitivity of a single-cone pinhole has been derived and compared to an equivalent double-cone geometry. The theoretical FWHM of the PRFs of the double-cone and single-cone pinhole PRFs were calculated based on previously published analytical resolution models, and were shown to be in good agreement with results obtained from Monte Carlo simulations using a realistic source model.

The penetrative sensitivity of the double-cone pinhole decreases more rapidly with horizontal displacement in comparison with the single-cone geometry. The greater penetrative sensitivity of the single-cone pinhole results in a larger direct photon flux on the detector, particularly for larger horizontal displacements.

The difference between the CoM of the projection from the Monte Carlo simulations and the true projected centre of the source was found to be similar for both pinhole geometries when the source was entirely contained within the FoV; however, a much greater difference was observed for the single-cone pinhole at the very edge of the field of view. Since the CoM of the projection will be used to estimate the projection of the centre of the source in *H*DR BrachyView, the double-cone pinhole will therefore enable more accurate source source tracking in *H*DR BrachyView.

Therefore, based on the analytical and simulation results for resolution, sensitivity and the accuracy of the estimated projected centre of the source, the double-cone pinhole collimator geometry is the most suitable choice for the *H*DR BrachyView probe.

References

[1] H. Deloar et al. “Evaluation of penetration and scattering components in conventional pinhole SPECT: phantom studies using Monte Carlo simulation”. In: *Phys Med Biol* 48.8 (2003), pp. 955–1008.

[2] C. Vanhove et al. “Three-pinhole collimator to improve axial spatial resolution and sensitivity in pinhole SPECT”. In: *Eur J Nucl Med Mol Imaging* 35.2 (2008), pp. 407–415.

[3] M. Safavi-Naeini et al. “BrachyView, A novel inbody imaging system for HDR prostate brachytherapy: Design and Monte Carlo feasibility study”. In: *Med Phys* 40.7 (2013).

[4] M. Petasecca et al. “BrachyView: Proof-of-principle of a novel in-body gamma camera for low dose-rate prostate brachytherapy”. In: *Med Phys* 40.4 (2013).

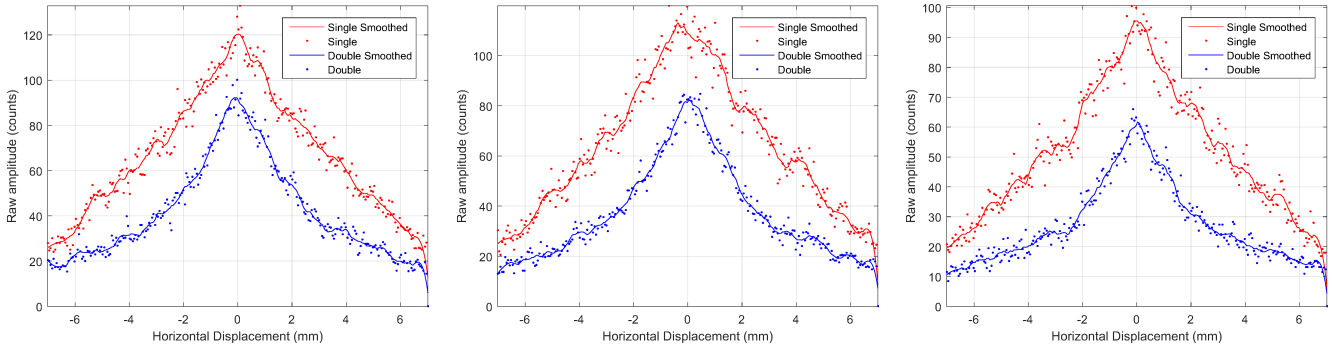

(a) $\theta = 90°,\ \phi = 0°$ (b) $\theta = 75°,\ \phi = 0°$ (c) $\theta = 60°,\ \phi = 0°$

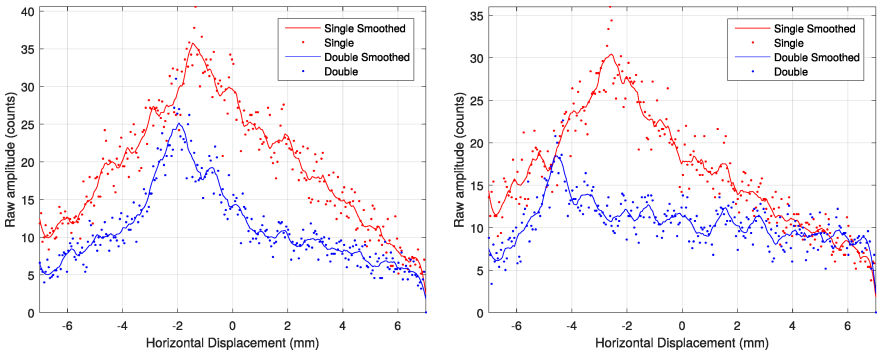

(d) $\theta = 75°,\ \phi = 90°$ (e) $\theta = 60°,\ \phi = 90°$

Fig. 10. PRFs obtained from simulations of double-cone and single-cone pinhole geometries for the five source positions. PRFs are measured across the centre of the projection image parallel to the x-axis and smoothed using a Savitsky-Golay filter.

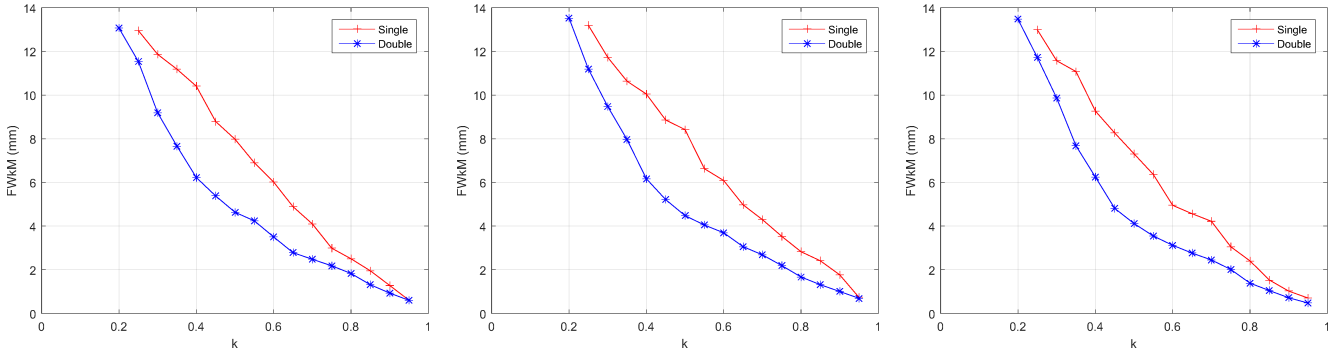

(a) $\theta = 90°,\ \phi = 0°$ (b) $\theta = 75°,\ \phi = 0°$ (c) $\theta = 60°,\ \phi = 0°$

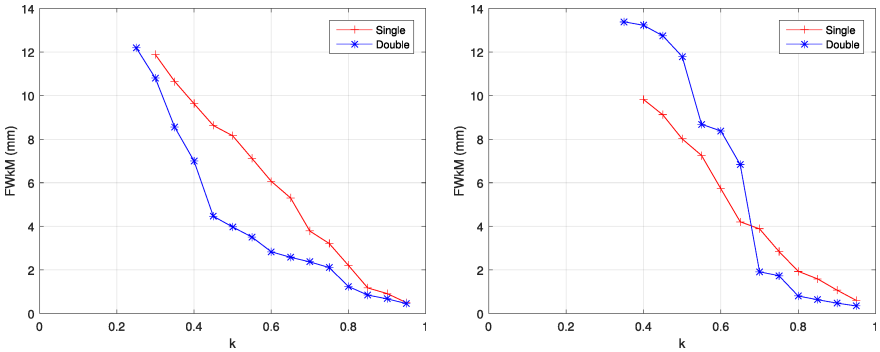

(d) $\theta = 75°,\ \phi = 90°$ (e) $\theta = 60°,\ \phi = 90°$

Fig. 11. FWkM calculated for k between 0.2 (and 0.25 for single-cone) and 0.95 for single-cone and double-cone pinhole geometries, computed from the simulated PRF profiles for $(\theta, \phi) = (60°, 0°)$, $(60°, 90°)$, $(75°, 0°)$, $(75°, 90°)$ and $(90°, 0°)$. For this geometry, FWkM could not be evaluated for small values of k due to the limited width of the detector.

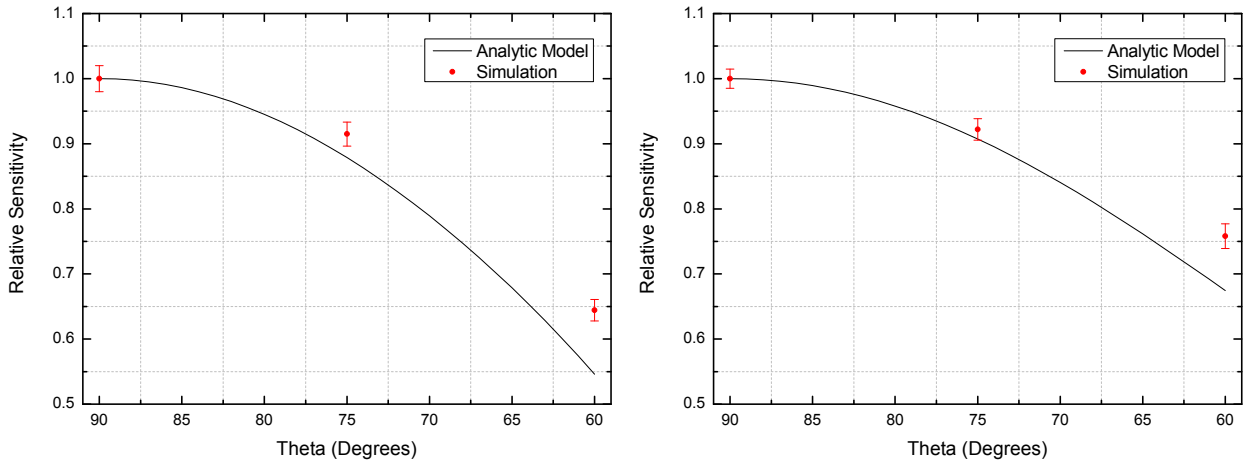

(a) Double-cone (b) Single-cone

Fig. 12. Penetrative sensitivity model validation of the analytical model using Monte Carlo simulations for double-cone and single-cone pinhole geometries normalised at $\theta = 90°$.

[5] R. Accorsi and S.D. Metzler. "Analytic Determination of the Resolution-Equivalent Effective Diameter of a Pinhole Collimator". In: *IEEE T Med Imaging* 23.6 (June 2004), pp. 750–763.

[6] S.D. Metzler et al. "Analytic Determination of Pinhole Collimator Sensitivity with Penetration". In: *IEEE T Med Imaging* 20.8 (Aug. 2001), pp. 730–741.

[7] F.P. Jansen, H. Qian, and D. Beque. "Efficient algorithm for modeling keel-edge pinhole response". In: *IEEE NSS/MIC Conf Rec*. Oct. 2009, pp. 3877–3881.

[8] P-C. Huang and C-H. Hsu. "Finite aperture modeling in small animal pinhole SPECT imaging". In: *IEEE NSS/MIC Conf Rec*. Vol. 6. Oct. 2004, pp. 3454–3457.

[9] G. Bal and P.D. Acton. "Analytical derivation of the point spread function for pinhole collimators". In: *Phys Med Biol* 51.19 (2006), p. 4923.

[10] Z. Han et al. "Radiation dose enhancement at tissue-tungsten interfaces in HDR brachytherapy". In: *Phys Med Biol* 59.21 (2014), p. 6659.

[11] M. Safavi-Naeini et al. "BrachyView, a novel in-body imaging system for HDR prostate brachytherapy: Experimental evaluation". In: *Med Phys* 42.12 (2015), pp. 7098–7107.

[12] R. Accorsi and S.D. Metzler. "Resolution-Effective Diameters for Asymmetric-Knife-Edge Pinhole Collimators". In: *IEEE T Med Imaging* 24.12 (Dec. 2005), pp. 1637–1646.

[13] H.O. Anger. "Radioisotope cameras". In: *Instrumentation in Nuclear Medicine*. Ed. by G.J. Hine. Vol. 1. New York: Academic Press, 1967. Chap. 19, pp. 485–552.

[14] X. Llopart et al. "Medipix2, a 64k pixel read out chip with 55 mu;m square elements working in single photon counting mode". In: *IEEE NSS/MIC Conf Rec*. Vol. 3. Nov. 2001, pp. 1484–1488.

[15] Z. Vykydal, J. Jakubek, and S. Pospisil. "USB interface for Medipix2 pixel device enabling energy and position-sensitive detection of heavy charged particles". In: *Nucl Instrum Meth A* 563.1 (2006), pp. 112–115.

[16] D. Rogers. *Monte Carlo models of Ir-192 sources*. National Research Council of Canada Ottawa. 1999.